JOURNAL OF Materials CHEMISTRY

Synthesis, structure and catalytic properties of Zr–Ce–Pr–O mixed oxides

Sylvie Rossignol,* Claude Descorme, Charles Kappenstein and Daniel Duprez

S. Rossignol, Laboratoire de Catalyse en Chimie Organique, UMR 6503, CNRS et Université de Poitiers, 40 Avenue du Recteur Pineau, 86022 Poitiers, France.
E-mail: Sylvie.rossignol@univ-poitiers.fr

Received 26th March 2001, Accepted 14th June 2001
First published as an Advance Article on the web 6th September 2001

$Zr_{0.10}(Ce_{1-x}Pr_x)_{0.90}O_2$ mixed oxides (x between 0 and 0.75) were prepared by coprecipitation (nitrates) or by the sol–gel route. Zirconium *n*-propoxide and cerium and/or praseodymium nitrates were used as precursors. "Sol–gel" oxides calcined at 900 °C were shown to be cubic with a fluorite-type structure. Coprecipated oxides could not be obtained as solid solutions. The BET surface area of these samples rapidly decreases when $x > 0.50$. A Raman study confirmed that all oxides were cubic and evidenced the presence of oxygen vacancies. The optimum oxygen storage capacity (OSC) was obtained for $Zr_{0.10}(Ce_{0.50}Pr_{0.50})_{0.90}O_2$. It appears that the substitution of cerium by praseodymium in $Zr_{0.10}Ce_{0.90}O_2$ mixed oxides leads to a material with improved redox properties. The presence of vacancies, associated with Pr^{3+}/Pr^{4+} ions, is thought to be responsible for these enhanced OSCs.

Introduction

Ceria (CeO_2) is a crucial component of modern automotive pollution control catalysts.[1] This oxide is a promoter in the water–gas shift reaction and prevents the sintering of the noble metals used as active centers. More important is the ability of this oxide to store oxygen. This phenomenon is associated with a fast Ce^{4+}/Ce^{3+} redox process in the solid, also involving anionic vacancies.[2–4] It was shown that up to 50% zirconium could be substituted for cerium into the ceria lattice to form solid solutions with face-centered cubic structures. In a previous work, we have evidenced that among the Zr–Ce–O mixed oxides, the compound $Zr_{0.1}Ce_{0.9}O_2$ prepared by the sol–gel procedure displays the highest oxygen storage capacity.[5,6]

Praseodymium is one of the possible "new" additives, which today attracts increasing attention. In fact, it was demonstrated that the oxygen exchange occurs at lower temperature on cerium–praseodymium mixed oxides than on ceria.[7] Furthermore, high temperature pretreatment does not affect the oxygen exchange capacity (OSC) of the mixed oxides. Moreover, high surface area PrO_y–ZrO_2 materials with a fluorite-type structure have also been prepared by the sol–gel procedure.[7,8]

The main objective of our study was to modify the composition of CeO_2 and $Zr_{0.10}Ce_{0.90}O_2$ samples, in order to follow the influence of cerium substitution by praseodymium and to enhance both thermal stability and oxygen storage capacity. The results will be discussed on the basis of DTA (differential thermal analysis), XRD (X-ray diffraction), Raman spectroscopy, BET surface area and OSC data.

Experimental

1 Preparation

Two series of samples were prepared. Series 1 consists of $Zr_{0.10}(Ce_{1-x}Pr_x)_{0.90}O_2$ samples while, in the second series ($Ce_{1-x}Pr_xO_2$), the oxide samples do not contain any zirconium. Preparation methods have been described earlier.[5] Solution concentrations were adjusted in order to synthesize 3 g of solid in each batch. All reactants were Aldrich products of 99% purity and were used without any further purification.

Sol–gel method (series 1). After dissolution in 20 cm^3 of isopropyl alcohol (Rhône–Poulenc, $H_2O \leqslant 0.5\%$), zirconium *n*-propoxide $Zr(OC_3H_7)_4$ (70% in propan-1-ol) precursor was slowly added (1 cm^3 min^{-1}, ambient temperature) to an aqueous solution containing $Ce(NO_3)_3{\cdot}6H_2O$ and $Pr(NO_3)_3{\cdot}6H_2O$ (20 cm^3, stirring speed: 500 rpm). A pseudo-gel forms immediately as the reactant mixture undergoes hydrolysis.

Coprecipitation method (series 2). Cerium–praseodymium oxides were prepared by co-precipitation. 12 cm^3 aqueous ammonia (14.7 mol L^{-1}) was slowly added to a mixture of $Ce(NO_3)_3{\cdot}6H_2O$ and $Pr(NO_3)_3{\cdot}6H_2O$ (both 20 cm^3 in distilled water). The precipitates were filtered off, re-dispersed in 100 cm^3 aqueous ammonia (0.25 mol L^{-1}) and filtered again.

The synthesized materials were dried in air at 60 °C for 1 h and at 120 °C overnight before further calcination in air at 900 °C for four hours.

Compared to coprecipitation, the major advantage of the sol–gel method is the possibility to prepare homogenous materials with a controlled composition at a nanometer scale. In this method, the structuring of the oxide proceeds by polymerization of molecular precursor entities. Small amounts of molecular precursor are sufficient to initiate polymerization. As a result, colloidal particles with 3D-structure are formed and further reticulation leads to the formation of the final gel. By contrast, precipitation upon addition of ammonia is more difficult to control; depending on the pK_a and solubility of the corresponding hydroxides and oxides, this method may lead to precipitates of various ill-defined compositions. Heterogeneous solids, in terms of both particle size and local composition, are finally obtained.[9]

2 Characterization

Differential thermal analysis (DTA) experiments were carried out in dry air (Air Liquide, $\leqslant 5$ ppm impurities) between 25 and 500 °C using a Thermal Analyst 2100 TA apparatus. Samples

previously dried at 120 °C were heated at 5 °C min^{-1}. Preliminary experiments showed that no DTA peak was observed above 500 °C.

Specific surface areas were determined by N_2 (Air Liquide, 30% N_2 in He) adsorption at −196 °C (one point BET method) with a Micromeritics Flow Sorb II.

XRD analysis was performed on a Siemens D500 powder diffractometer using Cu-Kα radiation (λ(Cu-Kα_1) = 0.15406 nm). Crystalline phases were identified by comparison with ICDD files [Pr_6O_{11}: 42-1121 (cubic); CeO_2: 34-394 (cubic)]. Standard diffractogram recording parameters were: dwell time = 1 s, step = 0.05°, 2θ range = 10–90°, divergence slit = 1°; for precise cell parameter determination: dwell time = 10 s, step = 0.02°. The diffraction peaks were fitted using the Profile program (Socabim, France) assuming a split pseudo-Voigt profile for peak fitting. U-Fit, a program developed by Evain (Institut des Matériaux de Nantes, France), was used for the determination of the precise cell parameters.[10]

Raman spectra were recorded using a Perkin Elmer spectrometer: Nd-YAG laser (1064.4 nm, 100 mW), dwell time = 120 s, number of scans = 20.

Oxygen storage capacity (OSC) was measured at 400 °C under atmospheric pressure. A 20 mg sample was continuously purged with helium (30 cm^3 min^{-1}). Successive or alternate pulses (0.265 cm^3) of O_2 (Air Liquide, $\leqslant$5 ppm total impurities) and CO (Air Liquide, N20) were injected every minute in order to simulate lean and rich operating conditions as those encountered in an Otto engine coupled with a three-way catalytic converter. The OSC was calculated from the CO consumption after stabilization of the sample in alternate pulses condition. A complete experiment on the $Zr_{0.10}(Ce_{0.50}Pr_{0.50})_{0.90}O_2$ sample of series 1 is described in Table 1. Successive CO injections induce the formation of CO_2 and the first CO pulse displays a good balance between consumption of CO and formation of CO_2. During subsequent CO pulses, a small part of the carbon monoxide molecules are trapped into the material and mole balance no longer applies. This carbon leftover is partially eliminated as CO_2 during the oxidizing treatment. Under alternate CO or O_2 pulses, CO_2 production and CO consumption are in good agreement. Furthermore, the O_2 uptake corresponds to a complete re-oxidation of the surface as is shown by eqns. (1) and (2):

$$2CeO_2(s) + 2yCO(g) \rightarrow 2CeO_{2-y}(s) + 2yCO_2(g) \quad (1)$$

$$2CeO_{2-y}(s) + yO_2(g) \rightarrow 2CeO_2(s) \quad (2)$$

The non-stoichiometric phase CeO_{2-y} can be better described as:

$$[Ce^{IV}_{1-2y}Ce^{III}_{2y}][O_{2-y}(V^{\circ\circ}_O)_y]$$

where $V_O^{\circ\circ}$ represents oxygen vacancies. Taking into account only the Ce ions reduced by CO, eqn. (1) can be rewritten in a more stoichiometric manner:

$$2Ce^{IV} + 4O^{-II} + CO(g) \rightarrow 2Ce^{III} + 3O^{-II} + V^{\circ\circ}_O + CO_2(g) \quad (3)$$

Therefore, eqn. (3) clearly evidences that the OSC involves only one oxygen atom out of four.

Table 1 Oxygen storage capacity measurement over $Zr_{0.10}(Ce_{0.50}Pr_{0.50})_{0.90}O_2$ (sample weight: 20 mg; pulses of 12 μmol of gas)

Step 1: 10 pulses CO followed by 10 pulses O_2

	Treatment under CO		Treatment under O_2	
Pulse number	CO consumed/ μmol g^{-1}	CO_2 formed/ μmol g^{-1}	O atoms consumed/ μmol g^{-1}	CO_2 formed/ μmol g^{-1}
1	257	257	592	8
2	198	194	10	0
3	89	75	0	0
4	29	17	0	0
5	20	9	2	0
6	16	6	0	0
7	15	4	0	0
8	15	4	0	0
9	13	0	0	0
10	13	0	0	0
Total	664	568	602	8

Step 2: alternate pulses of CO and O_2 (4 pulses of each gas)

Pulse number	CO consumed/ μmol g^{-1}	CO_2 formed/ μmol g^{-1}	O atoms consumed/ μmol g^{-1}	CO_2 formed/ μmol g^{-1}
1	306	300	325	0
2	346	308	246	0
3	288	281	288	0
4	284	276	286	0

Results

1 Structural characterizations (DTA, XRD, Raman)

DTA and XRD. After the drying step at 120 °C, all the samples correspond to complex mixtures containing mainly M^{III} (precursor oxidation state) with minor amounts of M^{IV} oxides and hydroxides (M = Ce or Pr) and no well-defined phase could be evidenced from the XRD results. Fig. 1 shows the thermograms obtained under air of all series 1 samples and of one series 2 sample ($x = 1$). All thermograms consist of endothermic peaks due mainly to the elimination of a weak quantity of the residual water molecules and to the transformation of hydroxide ions into oxide ions. Therefore, possible exothermic reactions such as the formation of a crystallized phase or the oxidation of Ce^{III} or Pr^{III} atoms are hidden by the endothermal events.

For $x = 0$ in series 1, the peak at 250 °C is characteristic of the appearance of a fluorite-type solid solution $Zr_{0.1}Ce_{0.9}O_2$.[6] For the other samples, this peak is shifted to higher temperature and additional endothermic peaks appear at lower temperatures.

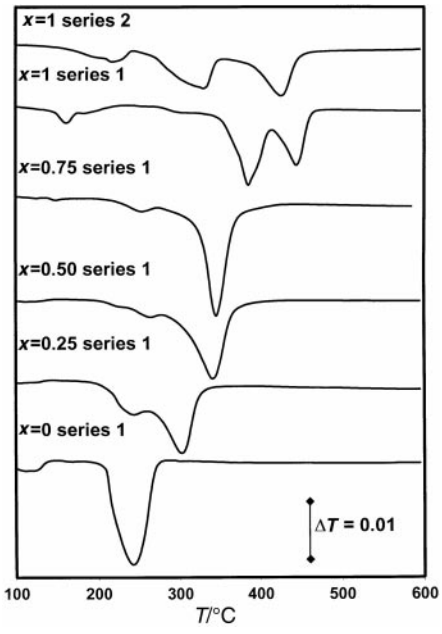

Fig. 1 DTA profiles of $Zr_{0.10}(Ce_{1-x}Pr_x)_{0.90}O_2$ oxides prepared by sol–gel (series 1) and $Ce_{1-x}Pr_xO_2$ oxides prepared by coprecipitation (series 2).

To understand these endothermic transformations, sample $Zr_{0.10}(Ce_{0.75}Pr_{0.25})_{0.90}O_2$ was studied in more detail using XRD measurements. This sample was successively calcined at 265, 370 (below and above the temperature at the maximum of the major endothermic peak) and at 900 °C for 4 h. The corresponding diffractograms are shown in Fig. 2(a). The particle sizes, determined from the FWHM (full width at half maximum) using the Scherrer relation are also reported. After calcination at 265 °C, the diffractogram is characteristic of a solid showing a fluorite-type structure.[5] Nevertheless, the line broadening indicates that the sample is not very well crystallized with the crystallite size being 6 nm. Calcination at 370 °C did not improve the degree of crystallization (Fig. 2(a)). After calcination at 900 °C, the peak width decreases, indicating a much higher crystallinity with a mean crystallite size of 16 nm. Consequently, the strongest endothermic peak can be associated with the formation of the fluorite-type solid solution. The increase in crystallite size occurs only between 400 and 900 °C and corresponds to a slow continuous process displaying no thermal event as the temperature increases. This process parallels a slow oxidation of the remaining Ce^{III} and Pr^{III} atoms as the cubic cell parameter decreases slightly from 5.424 to 5.392 Å (Fig. 2(a)); this small parameter change can be explained by two opposite effects: (i) a decrease in ionic radii when going from M^{3+} to M^{4+} cations (about 15 pm);[11] (ii) a concomitant increase of oxygen anions into the oxygen vacancies (see eqn. (4)):

$$4M^{3+} + 6O^{2-} + 2V_O^{\circ\circ} + O_2(g) \rightarrow 4M^{4+} + 8O^{2-} \qquad (4)$$

From our results, the first effect is predominant in agreement with the value of the cubic cell parameter of the praseodymium and cerium oxides (*vide infra*).

Therefore, for the series 1 samples with x in the range 0–0.75 (Fig. 1): the crystallization occurs in two steps:

(1) transformation of the initial mixture into a solid solution with fcc structure, small crystallite size and endothermic events;

(2) slow increase of crystallinity with no visible thermal event.

The temperature range of the transformation is shifted toward higher temperatures as the number of praseodymium atoms in the lattice increases (Fig. 1).

Diffractograms of the samples after calcination at 900 °C are displayed in Fig. 2(b) in the range 2θ 26–36°, including the calculated crystallite size. The series 1 samples (with x between 0 and 0.75) present only symmetrical diffraction peaks in agreement with the presence of one phase identical to $Zr_{0.10}Ce_{0.90}O_2$ ($x=0$) described in a previous paper.[5] This mixed oxide has been shown to be a solid solution with a fluorite-type structure and lattice parameter $a=5.3962$ Å. The lattice parameters of some samples are given in Table 2 and we observe a slight contraction of the cell as praseodymium atoms substitute for cerium atoms, in agreement with a smaller ionic radius for Pr^{4+}.[11] For the sample $Zr_{0.10}Pr_{0.90}O_2$ (Fig. 2(b), $x=1$, series 1) the distortion of the diffraction peaks indicates the presence of two phases: a major Pr_6O_{11} phase and a fluorite-type structure solid solution, in agreement with Sinev's work.[12]

In series 2, the oxides CeO_2 ($x=0$) and Pr_6O_{11} ($x=1$) appear to be single phase stable after air calcination at 900 °C. The non-stoichiometric praseodymium oxide can be better formulated:

$$[Pr_4^{IV}Pr_2^{III}][O_{11}^{-II}(V_O^{\circ\circ})_1]$$

which displays the importance of the vacancies.

For sample $Ce_{0.50}Pr_{0.50}O_2$ (series 2), a close look in the range 2θ 26–34° clearly evidences the presence of Pr_6O_{11} (Fig. 2(c)). Therefore, this sample prepared by coprecipitation, could not be obtained as a single phase mixed oxide as also found by Logan and Shelef using oxalate precursors.[13] By contrast, in the case of $Ce_{0.75}Pr_{0.25}O_2$, the presence of Pr_6O_{11} can be excluded on the basis of the XRD data.

For both series, the samples containing no cerium ($x=1$)

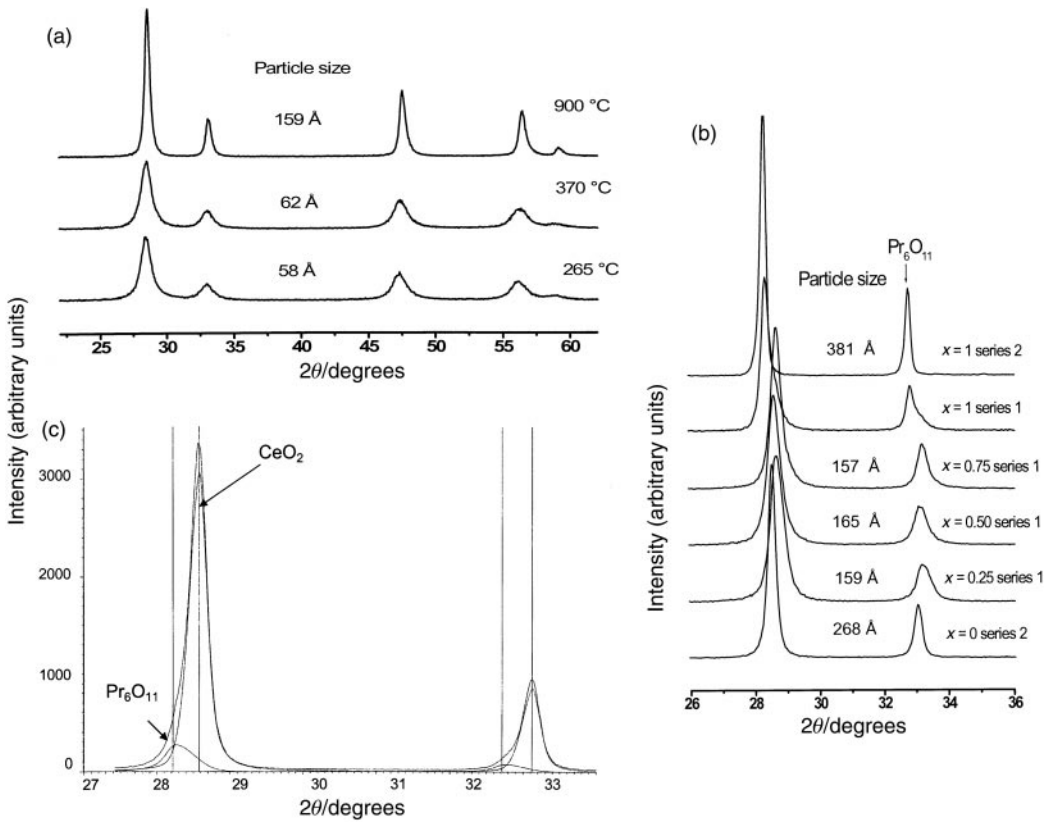

Fig. 2 (a): XRD patterns of the $Zr_{0.10}(Ce_{0.75}Pr_{0.25})_{0.90}O_2$ sample as a function of the calcination temperature. (b): XRD patterns of $Zr_{0.10}(Ce_{1-x}Pr_x)_{0.90}O_2$ oxides prepared by sol–gel (series 1) and $Ce_{1-x}Pr_xO_2$ oxides prepared by coprecipitation (series 2). (c): XRD profiles of $Ce_{0.50}Pr_{0.50}O_2$ oxide in the range 2θ 27–34° (deconvolution applied).

Table 2 Lattice parameters and experimental and calculated OSC

Series	Praseodymium fraction x	Lattice parameter/Å	OSC_{exp}/μmol CO g^{-1}	OSC_{calc}/μmol CO g^{-1}	OSC_{exp}/OSC_{calc}
Series 1: $Zr_{0.10}(Ce_{1-x}Pr_x)_{0.90}O_2$					
	$x=0$	5.3962	197	180	1.09
	$x=0.25$	5.3913	272	175	1.56
	$x=0.50$	5.3937	284	108	2.63
	$x=0.75$	5.3953	234	67	3.51
	$x=1$	Phase mixture	42	Not calculated	—
Series 2: $Ce_{1-x}Pr_xO_2$					
	$x=0$	5.4138	60	34	1.77
	$x=1$	5.4641	35	6	6.28

display different DTA profiles in comparison with the single phased samples (Fig. 1) and this behavior agrees well with the final presence of the praseodymium oxide phase Pr_6O_{11} and the successive formation of intermediate phases.[14]

Raman spectroscopy. Four Raman spectra only are presented in Fig. 3. For samples with x higher than 0.25, fluorescence effects due to praseodymium were so dominant that no spectra could be recorded. The band at *ca.* 460 cm^{-1} is attributed to the T_{2g} vibration mode of the metal–oxygen bond in the fluorite-type structure.[15–17] In the case of series 1 samples, the presence of this band confirms that these oxides are solid solutions. In order to explain the shift of this band as a function of x, samples were analyzed again after calcination at different temperatures (Fig. 4). This band is shifted towards higher frequencies as the calcination temperature increases (200, 400, 900 °C). This phenomenon could be related to structural ordering. By contrast, a shift towards lower frequencies can be observed as zirconium or praseodymium atoms substitute for cerium atoms. This shift indicates that the incorporation of Zr or Pr atoms induces a perturbation of the M–O bond involving some kind of disordering or structural distortion. McBride *et al.*[18] gave two reasons for the observed frequency shift: (i) an increase in the oxygen vacancy density and (ii) an expansion or contraction of the cell. In fact the presence of oxygen vacancies in this material could be explained by the presence of reducible praseodymium atoms (Pr^{4+}/Pr^{3+}). Moreover, in the case of $Ce_{0.75}Pr_{0.25}O_2$ (Fig. 3), a small and broad band appears at about 570 cm^{-1}. The same authors have tentatively attributed this band to the presence of oxygen vacancies in the material. In the other samples, this small band could not be observed. This fact can be linked either to the very weak intensity of the recorded spectra or to the absence of praseodymium in the oxide samples.

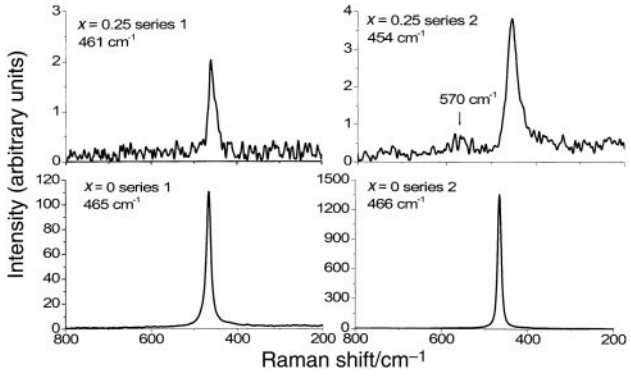

Fig. 3 Raman spectra of $Zr_{0.10}(Ce_{1-x}Pr_x)_{0.90}O_2$ and $Ce_{1-x}Pr_xO_2$ samples with $x=0$ and $x=0.25$ after calcination at 900 °C.

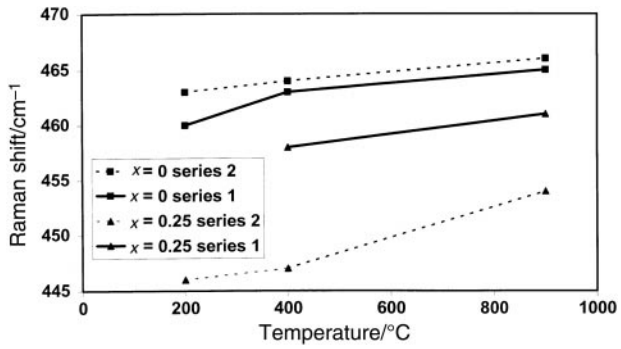

Fig. 4 Raman shift as a function of the calcination temperature for the two series of samples with $x=0$ and $x=0.25$.

Particle sizes. To compare XRD and Raman spectroscopic data, particle sizes were deduced from both types of measurements (Table 3). Particle sizes could be deduced from XRD patterns using the Scherrer relation,[19] and from Raman spectra using eqn. (5) established by Weber *et al.*:[16]

$$\Gamma = 5 + \frac{518}{D} \quad (5)$$

with:

D = particle size (Å)

Γ = full width at half maximum (FWHM) assuming a lorentzian profile for the Raman bands (cm^{-1}).

A good agreement is obtained between both sets of results. Nevertheless it remains difficult to discuss the effect on particle size of the introduction of both Zr and/or Pr atoms. We can remark, however, that the presence of zirconium leads to smaller size whereas the substitution of Ce by Pr is characterized only by minor effects.

2 Surface characterization and oxygen storage capacity

All BET surface areas are reported in Fig. 5. Whatever the series, introduction of Pr results in a decrease of the BET surface area. For series 1 samples, this decrease is even more pronounced for $x>0.5$. It seems that the presence of Pr_6O_{11} could be responsible for this decrease of surface area. Furthermore, the presence of zirconium remains crucial to stabilize cerium–praseodymium oxides: BET surface areas of series 1 samples are much higher than those of series 2, except for $x=1$. Praseodymium can stabilize the texture of ceria but its influence in obtaining high surface area oxides appears to be much weaker than in the case of zirconium addition.[2–4,20]

Table 3 Particle size determined from XRD and Raman measurements on the two series of samples

Series	Praseodymium fraction x	Calcination temperature/°C	XRD particle size/Å	Raman particle size/Å
1	$x=0$	200	45	44
		400	52	48
		900	145	138
	$x=0.25$	900	159	164
2	$x=0$	900	268	250
	$x=0.25$	900	85	63

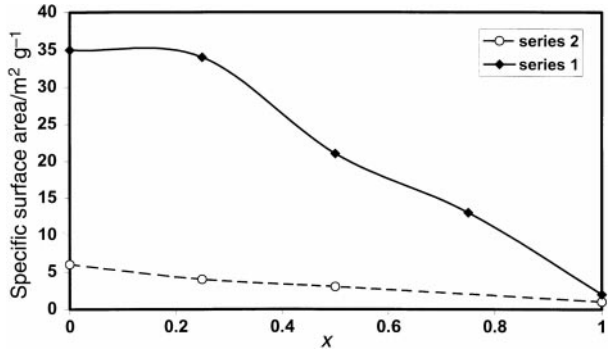

Fig. 5 Specific surface areas of $Zr_{0.10}(Ce_{1-x}Pr_x)_{0.90}O_2$ oxides prepared by sol–gel (series 1) and $Ce_{1-x}Pr_xO_2$ oxides prepared by coprecipitation (series 2) after calcination at 900 °C.

The evolution of the oxygen storage capacity (OSC/ μmol CO g^{-1}) is presented in Fig. 6 as a function of the amount of praseodymium in the solids. For both series, the introduction of praseodymium induces an increase of the OSC up to $x=0.50$, whereas above $x=0.50$ a decrease is observed. Therefore, an excess of praseodymium has a negative effect on the OSC.[21–23] In order to understand how praseodymium can influence the oxygen storage capacity, "calculated" OSC values were obtained as follows:

$$OSC_{cal} = \frac{bS}{Na^2} \quad (6)$$

with:

S = BET surface area ($m^2\ g^{-1}$)

a = lattice parameter (m)

N = Avogadro number

b = fraction of reducible elements (Ce + Pr) in the unit cell (0.9 for series 1, 1 for series 2)

This calculation is based on the following assumptions:

(1) all the Ce^{IV} or Pr^{IV} atoms of the surface monolayer are reduced to oxidation state III;

(2) the surface faces are {100} faces and contain 2 metal atoms and 4 oxygen atoms per unit surface area a^2 (a = cubic parameter); therefore one oxygen atom out of four participates in the OSC process as indicated by equation (3);

(3) oxygen atoms bonded to reducible elements are the only ones participating in the OSC.

Calculated and experimental values, expressed in μmol CO g^{-1}, are collected in Table 2. The ratio of these two values may represent the number of oxygen layers involved in the redox process. In all cases, calculated values are lower than the experimental ones. This observation shows that 2 to 3 layers are involved in the redox process. The increase of the OSC along with the amount of Pr shows that the presence of this element induces the creation of anionic vacancies. In fact, upon substituting for cerium cations, Pr ions may undergo a redox process (Pr^{3+}/Pr^{4+}) whereas this is not possible for zirconium cations.

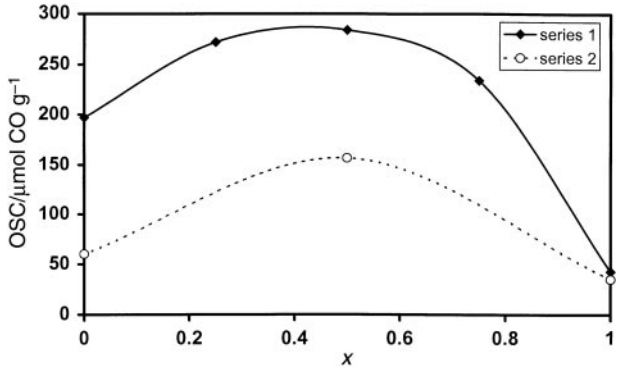

Fig. 6 OSC values measured at 400 °C as a function of x for the two series of samples calcined at 900 °C.

3 Thermodynamic considerations

In order to understand why praseodymium increases the OSC, the thermodynamics of CO reduction of the oxides present in our materials was investigated. The thermodynamic calculations were performed using the HSC code.[24] The Gibbs energies of the different cerium and praseodymium oxides, calculated at 673 K, are given in Table 4. For cerium oxides, the Gibbs energy of formation $\Delta_f G^\circ$ displays a continuous decrease as the oxidation state increases, thus showing that the stable phase at 673 K and 1 bar pressure of oxygen is clearly CeO_2. By contrast, for the praseodymium oxides a minimum is observed for $PrO_{1.72}$ and the more stable phases are therefore $PrO_{1.72}$ and $PrO_{1.83}$. The last oxide corresponds to the Pr_6O_{11} phase (11/6 = 1.833), in agreement with our results.

For cerium oxides samples, the first CO reduction step to $CeO_{1.83}$ can be written:

$$5.882CeO(s) + CO(g) \rightarrow CO_2(g) + 5.882CeO_{1.83}(s) \quad (7)$$

At 673 K, this reaction is endothermic ($\Delta_r H^\circ = 40.80$ kJ mol^{-1}) while the Gibbs energy change is slightly positive ($\Delta_r G^\circ = +10.37$ kJ mol^{-1}) which leads to an equilibrium constant:

$$K_p = \frac{P(CO_2)}{P(CO)} = 0.157$$

This pressure ratio corresponds to an extent of oxidation of 14% for CO during the pulse. The reduction of CeO_2 into the defined $CeO_{1.83}$ phase is thus possible for a single CO pulse. It must be emphasized, however, that the energy changes for the real surface reactions could be slightly different from the energy changes calculated for bulk phases; nevertheless the formation of ordered oxygen vacancies on the solid surface could favor the surface reduction of the oxide.

If we consider the reduction reaction of the praseodymium oxide (Pr_6O_{11} or $PrO_{1.833}$), we obtain eqn. (8), which leads to a very negative Gibbs energy ($\Delta_r G^\circ = -172.08$ kJ mol^{-1}).

$$3.003PrO_{1.833}(s) + CO(g) \rightarrow CO_2(g) + 1.502Pr_2O_3(s) \quad (8)$$

These results show clearly that praseodymium addition improves the cerium oxide reducibility as long as the solid solution is the sole phase. Nevertheless, excess praseodymium leads to the formation of a second praseodymium oxide phase Pr_6O_{11} and to a concomitant decrease of the reducibility which parallels the substantial reduction of the surface area (Fig. 5).

Conclusions

We prepared by the sol–gel route some thermally stable $Zr_{0.10}(Ce_{1-x}Pr_x)_{0.90}O_2$ mixed oxides (x between 0 and 0.75) with a fluorite-type structure. This structure was confirmed by the presence, in the Raman spectrum, of a single band at *ca.* 460 cm^{-1}, characteristic of the M–O vibration in the

Table 4 Gibbs energy G° and Gibbs energy of formation $\Delta_f G^\circ$ for some cerium oxides and praseodymium oxides at 673 K

Compound	G° at 673 K/kJ mol^{-1}	$\Delta_f G^\circ$ at 673 K/kJ mol^{-1}
$CeO_{1.5}$	−959.80	−800.57
$CeO_{1.72}$	−1052.87	−877.88
$CeO_{1.83}$	−1090.16	−907.28
CeO_2	−1142.21	−947.15
$PrO_{1.5}$	−968.47	−805.79
$PrO_{1.72}$	−1004.86	−826.83
$PrO_{1.83}$	−1009.58	−823.45
PrO_2	−1017.05	−818.95

fluorite-type structure. Moreover, the band position and the shoulder at 570 cm^{-1} indicate the presence of oxygen vacancies probably associated with praseodymium cations. Consequently, high OSCs appear to be the result of the presence of both cerium and praseodymium atoms. Thus, addition of praseodymium atoms into zirconia–ceria oxides appears to be very promising for the design of new automotive catalysts.

References

1 C. K. Narula, J. E. Allison, D. R. Bauer and H. S. Gandhi, *Chem. Mater.*, 1996, **8**, 984.
2 T. Bunluesin, R. J. Gorte and G. W. Graham, *Appl. Catal. B*, 1997, **14**, 105.
3 Y. Sun and P. A. Sermon, *J. Mater. Chem.*, 1996, **6**, 1025.
4 A. Trovarelli, F. Zamar, J. Llorca, C. Leitenburg, G. Dolcetti and J. T. Kiss, *J. Catal.*, 1997, **169**, 49.
5 S. Rossignol, F. Gerard and D. Duprez, *J. Mater. Chem.*, 1999, **7**, 1615.
6 S. Rossignol, Y. Madier and D. Duprez, *Catal. Today*, 1999, **50**, 261.
7 C. K. Narula, L. F. Allard and G. W. Graham, *J. Mater. Chem.*, 1999, **9**, 1155.
8 M. D. Krasil'nikov, I. V. Vinokurov and S. D. Nikitina, *Fiz. Khim. Electrokhim.*, 1979, **3**, 123.
9 A. Pierre, *Introduction au procédé sol–gel*, Forceram Septima, Paris, 1992.
10 M. Evain, IMN, Nantes, France, 1992.
11 N. N. Greenwood and A. Earnshaw, *Chemistry of the Elements*, 2nd edn., 1997, Butterworth–Heinemann, Oxford, UK, p. 1295.
12 M. Y. Sinev, G. W. Graham, L. P. Haack and M. Shelef, *J. Mater. Res.*, 1996, **11**, 1960.
13 A. D. Logan and M. Shelef, *J. Mater. Res.*, 1994, **9**, 468.
14 See ref. 11 p. 643.
15 S. Mochizuki, *Phys. Status Solidi B*, 1982, **114**, 189.
16 W. H. Weber, K. C. Hass and J. R. McBride, *Phys. Rev. B*, 1993, **48**, 178.
17 G. Groppi, C. Cristiani, L. Lietti, C. Ramella, M. Valentini and P. Forzatti, *Catal. Today*, 1999, **50**, 399.
18 J. R. McBride, K. C. Hass, B. D. Poindexter and W. H. Weber, *J. Appl. Phys.*, 1994, **76**, 2435.
19 H. Keijser, J. I. Langford, E. J. Mittemeijer and A. B. P. Vogels, *J. Appl. Crystallogr.*, 1982, **15**, 308.
20 S. Imamura, J. I Tadani, Y. Saito, Y. Okamoto, H. Jindai and C. Okamoto, *Appl. Catal. A*, 2000, **201**, 121.
21 G. Balducci, J. Kaspar, P. Fornasiero, M. Graziani and M. Saiful Islam, *J. Phys Chem. B*, 1998, **102**, 557.
22 L. Mubmann, D. Lindner, E. S. Lox, R. Van Yperen, T. P. Kreuser, I Mitsushima, S. Taniguchi and G. Garr, *SAE Technical Paper* 970465, 1997.
23 C. Leitenburg, A. Trovarelli, F. Zamar, S. Maschio, G. Dolcetti and J. Llorca, *J. Chem. Soc., Chem. Commun.*, 1995, 2181.
24 HSC Chemistry V4.1, Outokumpu Oy, Pori Finland, A. Roine.